Thin Solid Films 622 (2017) 78–83

Contents lists available at ScienceDirect

Thin Solid Films

journal homepage: www.elsevier.com/locate/tsf

Growth and characterization of Au nanoparticles embedded In_2O_3 composite films

M.R. Ananthan [a,1], P. Malar [b,d], Thomas Osipowicz [b], Shikha Varma [c], S. Kasiviswanathan [a,*]

[a] Thin Films Laboratory, Department of Physics, Indian Institute of Technology Madras, Chennai 600 039, India
[b] Centre for Ion Beam Applications, Department of Physics, National University of Singapore, Singapore
[c] Institute of Physics, Bhubaneshwar 751 005, India
[d] Research Institute, Department of Physics and Nanotechnology, SRM University, Kattankulathur, Chennai, India

ARTICLE INFO

Article history:
Received 29 December 2015
Received in revised form 5 November 2016
Accepted 6 December 2016
Available online 9 December 2016

Keywords:
Au nanoparticles
Nano composites
In_2O_3:Au
Persistent photoconductivity

ABSTRACT

Au nanoparticles embedded In_2O_3 thin films (In_2O_3:Au) were grown by DC reactive sputtering method in three different target configurations. Presence of Au in In_2O_3 matrix was confirmed by glancing angle X-ray diffraction (GXRD) and transmission electron microscopy (TEM). Crystallite sizes of Au were obtained by Debye-Scherrer formula from GXRD data. Localized surface plasmon resonance was observed for In_2O_3:Au samples from optical absorption measurement at peak value of ~550 nm and inferred red shift of resonance peak towards the increasing crystallite size. Rutherford backscattering spectrometry (RBS) studies of selected samples on Si substrate showed minor In diffusion and absence of Au diffusion into the Si substrate. X-ray photoelectron spectroscopy (XPS) studies revealed that the chemical state of Au is neutral. The samples with high Au content exhibited persistent photoconductivity due to the sub band gap absorption indicating the introduction of sub band gap trap levels in In_2O_3.

1. Introduction

Metal nanoparticles exhibit properties that differ significantly from those of their bulk counterpart and are attractive from scientific and technological points of view [1,2]. For instance, noble metal nanoparticles, display pronounced absorption caused by collective excitation of conduction electrons called localized surface plasmon resonance [2]. Noble metal nanoparticle embedded thin films are a rigorous area of research due to their unique functional properties. The main properties of interest are optical, catalytic, electrical/thermal conductivity, antibacterial/biological, colour, photocatalysis, photochromic effects, electrochromic, photoluminescence, the plasmon resonance/shift and enhanced reactivity [3–5]. The properties expected from noble metal nanoparticles embedded system are due to the noble metal nanoparticles morphology, shape, size and the dielectric nature of the surrounding medium. When the embedded medium becomes a transparent conducting oxide (TCO), they generally exhibit unique combination of two characteristics, viz., high optical transparency and large electrical conductivity. Therefore metal nanoparticle embedded TCO films are expected to possess interesting characteristics. For instance, the plasmon band that appears in the visible region can be wavelength shifted and hence nanoparticles embedded thin films may be used as filters. Further, silver nanoparticles embedded indium tin oxide thin films [6] have shown large enhancement in electrical conductivity. In addition, noble metal nanoparticle embedded oxide films have been found to show large non-linear optical coefficients [7–9]. These above observations are inspiring towards the strong research on metal nanoparticles embedded transparent oxide thin films.

TCOs are heavily doped large band gap semiconductors which possess high optical transparency (~85%) and high electrical conductivity ($10^4\ \Omega^{-1}\ cm^{-1}$), which are, in general, considered as diametrically opposite characteristics [10–13]. High optical transparency is due to the large optical gap (>3 eV) while electrical conduction has been attributed to oxygen vacancies. They are metal oxides and hence show n-type conduction due to oxygen deficiency. The three well known oxides are In_2O_3, SnO_2 and ZnO [14]. TCO thin films are primarily used as transparent electrodes in solar cells, flat panel displays, sensors and other devices, which need to be transparent for visible light [15–17]. Indeed, Au nanoparticles are the most stable metal nanoparticles due to the inert nature of Au similarly In_2O_3 is a well-known TCO. The resistivity of In_2O_3 can be varied by even ten orders by introducing oxygen vacancies, which is needed for studying the metal nanoparticles in different conducting environment. The present article narrates the preparation

* Corresponding author.
E-mail addresses: mrananthan@gmail.com, ananthan@kce.ac.in (S. Kasiviswanathan).
[1] Present address: Karpagam College of Engineering, Myleripalayam, Coimbatore, Tamil Nadu, India.

http://dx.doi.org/10.1016/j.tsf.2016.12.009
0040-6090/

and some of the physical properties of Au nanoparticles embedded In_2O_3 thin films.

2. Experiments, results and analysis

2.1. Growth of In_2O_3:Au thin films

In_2O_3:Au thin films were grown by dc reactive sputtering of a In-Au composite target. It consists of a 3 inch diameter 5 N purity In disc with small 5 N purity Au discs placed on its surface at suitable locations. The Au content in the films was varied by altering the number and the size of the Au discs. Three different target configurations were used: 1) Two 8 mm diameter Au discs placed diametrically opposite to each other at a distance of 29 mm from the centre, 2) A 8 mm diameter Au disc kept at the centre, and 3) A 4 mm diameter Au disc kept at the center. Hereafter, films obtained using these three configurations are called as sample A, sample B and sample C respectively, for brevity of presentation. The other sputtering conditions are same as those used for growing In_2O_3 films. Briefly, sputtering was done at a constant power (100 W) using a gas mixture consisting of 98% Ar and 2% O. The pressure during sputtering was 5×10^{-2} mbar. After deposition, the films were annealed at 673 K for a period of 3 h in flowing argon prior to making any measurements. It is to be mentioned here that the resistivity of In_2O_3:Au thin films were nearly three orders higher than that of In_2O_3 thin films, deposited under similar conditions. This indicates that during sputtering the oxygen content in the films increases.

2.2. GXRD studies

GXRD measurements were carried out in a PANalytical (model: X'Pert PRO) XRD unit using Cu-K_α radiation. Fig. 1a–c show typical GXRD patterns obtained for samples A, B and C respectively. The patterns observed for sample A (Fig. 1a) and sample B (Fig. 1b) contained peaks that could be identified with those of In_2O_3 and Au. Among the peaks, only two have been found to arise from Au and correspond to reflections from (111) and (200) planes (JCPDS card no.:004-0784). However, GXRD pattern of sample C (Fig. 1c) did not show evidence for the presence of Au, which may be attributed to the low concentration of Au.

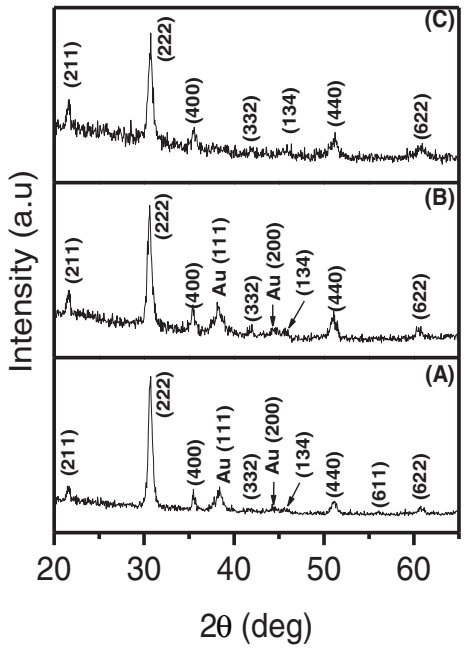

Fig. 1. GXRD pattern of In_2O_3:Au thin films. Panels a, b and c correspond to samples A, B and C respectively.

The average Au crystallite sizes, calculated using Debye-Scherrer formula [18] for samples A and B are ~12 nm and ~9 nm respectively.

2.3. TEM studies

In_2O_3:Au thin films were subjected to TEM investigations for detailed structural analyses. TEM measurements were performed using Philips CM-12 equipment. In TEM, plane-view electron micrograph gives information about the microstructure of the sample and selected area diffraction (SAD) pattern reveals the crystalline nature. The accelerating potential was kept at 80 kV and the electron beam current during the experiments was ~1 μA. TEM measurements were made on sample C, as it was not possible to identify the presence of Au from

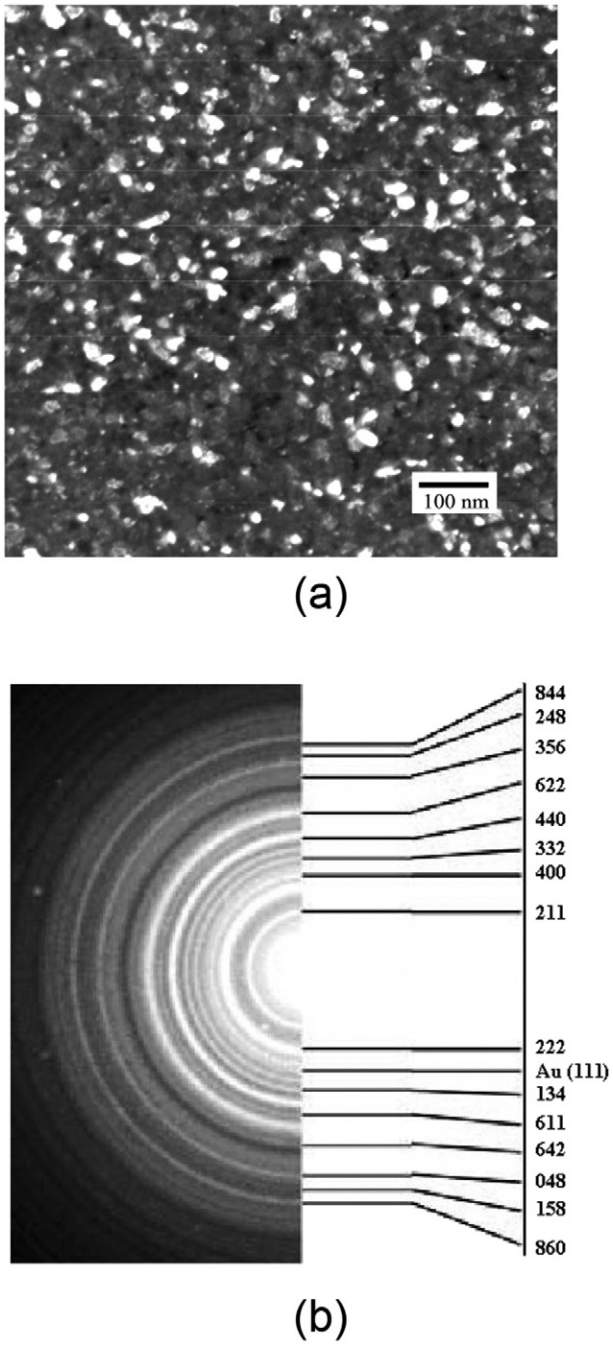

Fig. 2. (a) TEM micrograph of In_2O_3:Au thin film (sample C) and (b) the corresponding electron diffraction pattern. Ring corresponding to reflection from Au (111) plane is also marked.

GXRD patterns. Fig. 2a shows a dark field electron micrograph of sample C. The accelerating potential and the beam current used were 80 kV and 1 μA respectively. The polycrystalline nature of the In_2O_3:Au film can be clearly seen in the micrograph. However, it is not possible to differentiate Au crystallites from those of In_2O_3 matrix. The corresponding indexed SAD pattern is displayed in Fig. 2b. The sharp rings present in the SAD patterns confirm the polycrystalline nature of the film. In addition to the reflections from different In_2O_3 planes, the diffraction pattern also contains a ring due to the reflection from Au (111) plane, which confirms the presence of Au crystallites in the film. The ring due to Au (111) plane also indicate that Au crystallites are predominantly oriented along the [111] direction.

2.4. Optical absorption studies

Optical absorption measurements were made on In_2O_3:Au thin films deposited on glass substrates. Absorbance spectra were recorded in the wavelength range of 300 to 2400 nm using Jasco V 570 UV–VIS–NIR spectrophotometer. Optical absorbance spectra of In_2O_3:Au thin films are shown in Fig. 3. The curves marked by letters a, b and c correspond to samples A, B and C respectively. The spectral response of absorbance of pure In_2O_3 thin film (deposited without Au nanoparticles) is also shown in Fig. 3 (marked In_2O_3), for the purpose of comparison. The steep rise exhibited by all the spectra below a wavelength of about 350 nm, is due to the fundamental absorption edge of In_2O_3, which has a band gap of ~3.75 eV.

It can be seen from Fig. 3 that the In_2O_3:Au films exhibit distinct absorption maxima in the range 540 to 565 nm, typical of localized surface plasmon resonance (LSPR) due to Au nanoparticles [19]. The presence of absorption maximum due to LSPR in sample C confirms the presence of Au nanoparticles. Sample A has got the highest absorption maxima due to LSPR while sample C has got the least value, which shows that the strength of LSPR absorption decreases as the concentration of the Au nanoparticles decreases in the films. The position of the LSPR absorption maximum is determined mainly by the size of nanoparticles, their shape, inter-particle spacing and the dielectric function of the matrix in which they are embedded [20]. The absorbance maxima occurs at 564 nm, 552 nm and 546 nm respectively for the samples A, B and C, indicating that the plasmon band shifts towards the longer wavelengths as the Au content is increased in the films. The contribution to the shift from dielectric function can be ruled out in the present case, as the dielectric function of the medium (In_2O_3) is not expected to change with concentration of nanoparticles. The effect of inter-particle spacing on LSPR position has been observed in nanoparticle pairs. It is attributed to the change in dipolar coupling and depends on the state of polarization of the incident light as well [21]. The LSPR maximum exhibits red-shift for light polarized parallel to the inter-particle axis, whereas for light polarized normal to the inter-particle axis, it shows blue-shift. In the present case, since the particles are expected to be distributed randomly with different sizes, inter-particle separation is unlikely to have significant influence on the LSPR shift. A possible reason for the observed red-shift may be the nanoparticle size, as the effect of radiation damping increases with enhancement of particle size. In fact, similar red-shift due to particle size has been observed in earlier studies on noble metal nanoparticles embedded SiO_2 films [22].

2.5. RBS studies

Rutherford backscattering spectroscopy (RBS) measurements were carried out using the 3 MV singletron accelerator at the Centre for Ion Beam Applications at the National University of Singapore [23]. A 2 MeV He^+ beam of typically 20 nA beam current and 1 mm^2 spot size was used. RBS spectra were analyzed using the "XRUMP" simulation code [24]. RBS measurements have been made using $4He^+$ ions on all the samples and the results of sample B alone has been chosen for discussion for the sake of brevity. Fig. 4 shows a typical RBS spectra of In_2O_3:Au thin film deposited on Si together with the simulated curve. Experimental data points and the simulated curve are denoted by open circles and continuous line respectively. The front edges of Au and Si appear at channel numbers of about 1300 and 700 respectively. The back edge of In appears at a channel number of about 1000. Yield due to O appears as a super imposed peak on Si plateau.

Simulations were started with an initial sample configuration of a thin layer on a thick substrate. The simulation that reproduced the experimental data well yielded a three layer configuration. The first layer was found to be that of In_2O_3:Au thin film and consisted of In, O and Au with atomic percentages of 38.0, 55.2 and 6.8 respectively. The ratio of atomic percentages of In to O was slightly higher than that was observed for pure (without Au nanoparticles) In_2O_3, grown under similar conditions. The next layer was a thin interface layer formed between In_2O_3:Au thin film and the substrate. It consisted of In, O and Si with atomic percentages of 27.5, 42.7 and 29.8 respectively. The formation of this layer may be attributed to the striking of the substrate by secondary electrons during sputtering. The interface layer does not contain Au and therefore any Au present must be below the limit of detection of the present measurements.

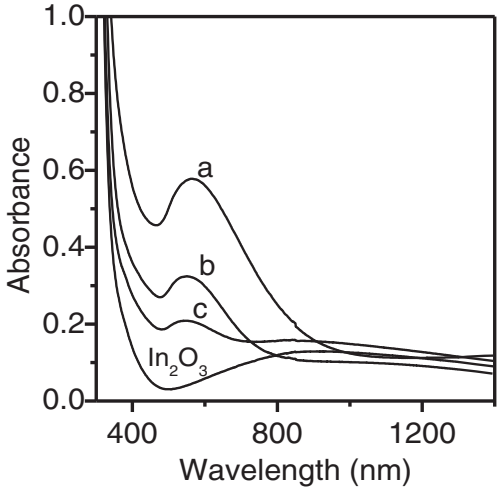

Fig. 3. Optical absorption spectra of In_2O_3:Au thin films. The spectra of samples A, B and C are marked a, b and c respectively. The spectra of In_2O_3 thin film (marked In_2O_3) is also shown for the sake of comparison.

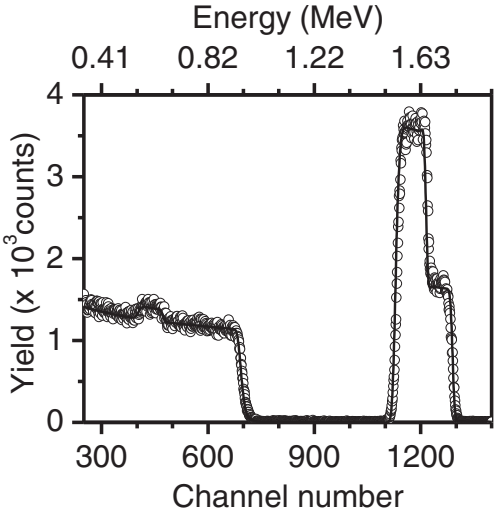

Fig. 4. RBS spectra of In_2O_3:Au thin film grown on Si.

2.6. XPS studies

Photoelectron spectra were obtained with a ESCA-2000 Multilab apparatus (VG Microtech) available at Institute of Physics Bhubaneshwar, India. A non-monochromatic Mg K_α excitation source and a hemispherical analyzer were used for the measurements. Residual gas pressure in the chamber during the measurements was ~10^{-10} mbar. All spectra were recorded at 90° take-off angle with a pass energy of 20 eV and at an instrumental resolution of 0.9 eV. After obtaining a survey scan in the energy range 0 to 1000 eV, core level spectra of elements were recorded for the films. The binding energies were corrected with reference to the C 1s line at 284.6 eV. The In_2O_3:Au thin films displayed certain interesting characteristics which prompted the XPS study of the valence state, especially of Au. The resistivity of In_2O_3:Au thin films were much higher than that of In_2O_3 films without Au nanoparticles, but otherwise grown under identical conditions. The increase in resistivity suggests to study the nature of valance state of Au in In_2O_3 matrix. Determination of the valence state of Au can reveal if new trap levels are created by Au impurities of In_2O_3 which consequences any unusual photoconductivity behavior.

Fig. 5 shows a typical XPS survey scan spectra of In_2O_3:Au thin film (sample B) measured in the energy range of 0 to 1000 eV. Various peaks in the spectra are indexed and correspond to different levels of the elements present on the surface of the film. The presence of C peak is due to the exposure of the film to atmosphere. Fig. 6 a–c show the core level spectra of Au 4f, In 3d and O 1s respectively, on an expanded scale. The experimental data points, fits to individual peaks, and the overall fit to the spectra are denoted respectively by open circles, grey lines and black lines respectively. Peak fitting was done after subtracting a Shirley background.

Photoemission spectra of Au 4f core level exhibited a doublet, fitting of which yielded binding energies of 83.9 and 87.6 eV for the spin-orbit $4f_{7/2}$ and $4f_{5/2}$ states. These values match very well with the reported values of Au^0 state [19], which signifies that Au in In_2O_3 matrix is in neutral state. Hence, In_2O_3:Au thin films can be considered as a heterogeneous system consisting of a mixture of Au nanoparticles and In_2O_3. Analysis of In 3d core level spectra yielded the binding energies of spin-orbit split $3d_{5/2}$ and $3d_{3/2}$ states to be 444.8 eV and 452.4 eV, respectively. These values are close to those reported for In present in bulk In_2O_3 [25–27] and confirm that the formal valence of In is 3^+. The deconvoluted O 1s core level spectra showed the presence of two peaks at 530.2 and 531.8 eV respectively. The peak 530.2 may be assigned to O in crystalline In_2O_3, while the latter at 531.8 eV may be assigned to the adsorbed OH species [25–27]. It may be concluded from the results of photoemission spectra that Au is in the neutral sate and the formal valence states of In and O are same as those expected for In and O in bulk In_2O_3.

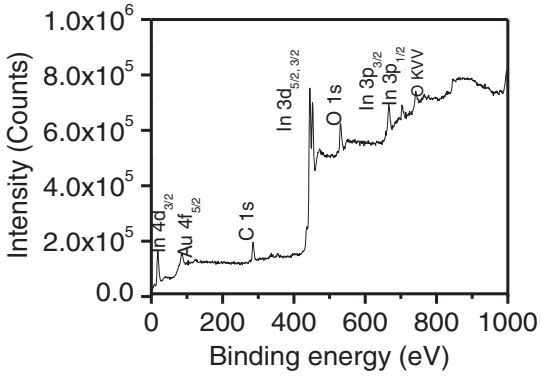

Fig. 5. Typical photoemission survey scan spectra of In_2O_3:Au thin films.

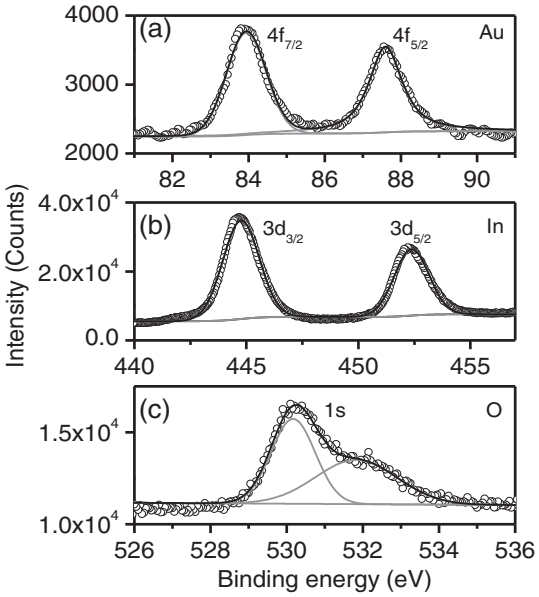

Fig. 6. Core level spectra of different elements of In_2O_3:Au thin films. a) Au 4f, b) In 3d and c) O 1s.

2.7. Photocurrent studies

In_2O_3:Au thin films showed persistent photocurrent when illuminated with a blue LED source (peak wavelength ~ 490 nm). The photo current was observed for specified wavelength range and excitation with longer wavelength sources (Green, Yellow and Red) did not result in any change. Photocurrent measurements were made at room temperature using a two probe method. Prior to the measurements, the films were kept in dark for long. Fig. 7 shows the evolution of photocurrent as a function of time. Measurements were started immediately after the LED's were switched on (marked as LED ON) and continued for about 2 h after they were switched off (marked as LED OFF). The photocurrent build-up as well as decay occur over a long period of time. As can be seen from Fig. 7, the photocurrent do not saturate within the time window over which the measurements were made.

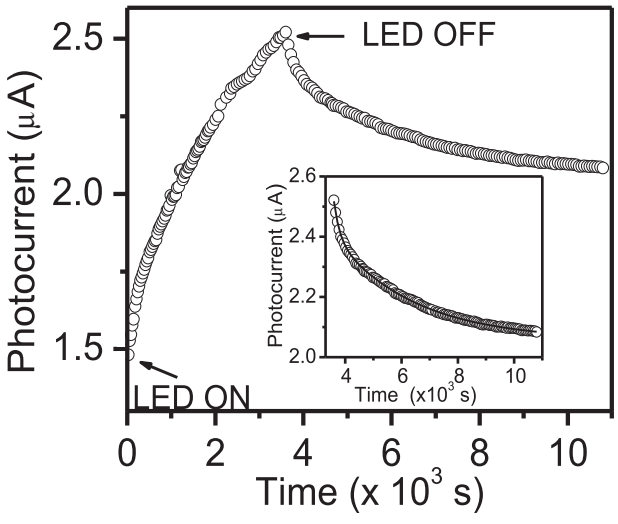

Fig. 7. Built-up and decay of photocurrent. The arrows indicate the instants at which the excitation source was turned on and off. The inset shows the decay part of the measured photocurrent (symbols) along with the least square fitted curve (continuous line).

The photocurrent decay, in general, can be modeled using a simple exponential decay function with single time constant. In the present case, the photocurrent decay data could not be fitted with a single exponential but needed two exponential transients given by,

$$I(t) = I_1 \exp(-t/\tau_1) + I_2 \exp(-t/\tau_2) \quad (1)$$

where, τ_1 and τ_2 are the two time constants, which signify two different rate processes. The inset to Fig. 7 shows the experimental photocurrent data (open circles) together with the least square fitted curve (continuous line through the data points). The extracted time constants are found to differ by an order of magnitude with values of 2.5×10^2 and 2.9×10^3 s. The large time constants are indicative of the deep trap levels in the forbidden gap of In_2O_3. The time needed for the carriers to escape from the trap level depends on the position of the trap level. In fact, for a given temperature, it varies exponentially with the trap level energy [28] and can be written as,

$$\ln(\tau/\tau_0) = E_t/k_B T \quad (2)$$

Here, $\tau_0 = 1/\nu_0$, where, ν_0 is the attempt frequency and is taken as 10^{13} Hz, the vibrational frequency of the lattice [29]. E_t is the energy of the trap level, measured from the top of the valence band, k_B is the Boltzmann constant and T is the temperature. The calculations have yielded the values of trap levels to be 0.91 eV and 0.98 eV, corresponding to time constants 2.5×10^2 and 2.9×10^3 s respectively.

Persistent photocurrent is an excess current resulting from change in free carrier density mediated by sub-band gap light and persists long after the excitation source is switched off. It is observed in several semiconductors, in particular compounds and solid solutions of III-V and II-VI semiconductors and metal oxides [30,31]. Persistent photocurrent is usually associated with deep levels that serve as recombination centers for electron-hole pair [32]. The defects may be present in the bulk for single crystals or in the grain boundary, if the solid is polycrystalline. A metastable defect that is often considered responsible for persistent photocurrent is the DX center (D-stands for donor and X specifies that the defect is unknown, which is the case quite often) [33–36]. The DX center, depending on its state, plays a dual role of deep level with highly localized wave function or a shallow level with hydrogen like wave function and hence can contribute to conduction. An example of DX center is the oxygen vacancy in ZnO, which in its unionized neutral form, creates a deep level that cannot contribute to conductivity [33,37]. When it is doubly ionized with a light of suitable energy, a large outward lattice relaxation takes place and as a result, it forms a shallow state below the conduction band. When light is switched off, the difference in lattice relaxations presents a barrier (~0.2 eV) for electron capture by the deep level, which results in persistent photocurrent. Distortion in the lattice has also been known to increase the decay time. For instance, in InGaN, random potential fluctuation arising from compositional fluctuation was shown to decrease the trap capture rate [38] while fluctuation resulting from strain due to lattice mismatch in GaN was found to be responsible for increasing the decay time [39].

Reports of photoresponse of amorphous [40], micro-crystalline [41] and polycrystalline In_2O_3 thin films [42] to UV radiation are available in the literature. The films exhibited considerable reduction in resistivity, which could be reverted to its initial value. The reversible changes in resistivity were attributed to reduction by UV light and subsequent oxidation in ozone rich atmosphere. It has been shown [43] that the changes are confined to a very thin surface region and not in the bulk of the film. There has been no previous experimental evidence for persistent photocurrent in In_2O_3. Tanaka et al. [43] have performed theoretical calculations on neutral vacancies in Al_2O_3 and In_2O_3. They have observed that neutral O vacancy can form shallow level. Doubly ionized O vacancies are known to form shallow donor levels and in fact, they are responsible for the n-type conductivity in off-stoichiometric In_2O_3, which is a semi-insulator in its stoichiometric form [12]. More recently, Lany and Zunger [34] based on their work on ZnO, have suggested that neutral oxygen vacancies in In_2O_3 can give rise to deep localized states. Therefore, we understand, in the present case the deep trap level may be created due to neutral oxygen vacancies. Since neutral oxygen vacancies in metal oxides (e.g. ZnO) create deep levels that trap electrons, the resistivity of the films will be high. In fact, we have observed that for given sputtering conditions, the In_2O_3:Au film exhibited resistivity which is nearly three orders of magnitude higher than that of In_2O_3 films ($\sim 10^{-3}$ Ω cm [44]) without Au nanoparticles. A possible reason for the creation of neutral vacancies may be the bombardment of the substrate by secondary electrons and other species in the plasma during sputtering. In fact, electron irradiation has been suggested to be responsible for the creation of neutral O vacancies in ZnO films [37]. However, the actual cause for the creation of neutral oxygen vacancies during co-sputtering is unclear now and needs further studies.

3. Conclusion

In_2O_3:Au films have been grown by co-sputtering. GXRD and TEM studies revealed the Au crystallites orientation along [111] direction. Presence of Au nanoparticles in the films has been confirmed by the absorption band due localized plasmon resonance in the optical spectra. XPS results showed that Au is in neutral state. The films exhibited persistence photocurrent and is attributed to the presence of deep levels.

References

[1] U. Kreibig, M. Vollmer, Optical Properties of Metal Clusters, Vol. 13, Springer-Verlag, Berlin, 1995.
[2] C.D. Geddes (Ed.), Reviews in Plasmonics 2015, Springer Science, New York, 2016.
[3] P. Bamfield, M.G. Hutchings, Chromic Phenomena: Technological Applications of Colour Chemistry, second ed. RSC Publications, Cambridge, 2010.
[4] P.C. Lombardo, A.L. Poli, L.F. Castro, J.R. Perussi, C.C. Schmitt, Photochemical deposition of silver nanoparticles on clays and exploring their antibacterial activity, ACS Appl. Mater. Interfaces 8 (2016) 21640–21647.
[5] R. Bawa, G.F. Audette, I. Rubinstein (Eds.), Hand Book of Clinical Nanomedicine: Nanoparticles, Imaging, Therapy and Clinical Applications, CRC Press, Boca Raton, 2016.
[6] B. Houng, Tin doped indium oxide transparent conducting thin films containing silver nanoparticles by sol-gel technique, Appl. Phys. Lett. 87 (2005) 251922.
[7] I.V. Kityk, A. Ali Umar, M. Oyama, Circular acoustogyration effect on gold nanoparticles grown on indium tin oxide, Appl. Opt. 44 (2005) 6905–6909.
[8] A.I. Ryasnyansky, B. Palpant, S. Debrus, R.I. Khaibullin, A.L. Stepanov, Nonlinear optical properties of copper nanoparticles synthesized in indium tin oxide matrix by ion implantation, J. Opt. Soc. Am. B 23 (2006) 1348–1353.
[9] C. Yang, W. Ow, Y. Shigesato, D.C. Paine, Interfacial stability of an indium tin oxide thin film deposited on Si and $Si_{0.85}Ge_{0.15}$, J. Appl. Phys. 88 (2000) 3717–3723.
[10] K.L. Chopra, S. Major, D.K. Pandya, Transparent conductors-a status review, Thin Solid Films 102 (1983) 1–46.
[11] I. Hamberg, C.G. Granquist, Evaporated Sn-doped In_2O_3 films: basic optical properties and applications to energy-efficient windows, J. Appl. Phys. 60 (1986) R123–R159.
[12] T. Minami, Transparent conducting oxide semiconductors for transparent electrodes, Semicond. Sci. Technol. 20 (2005) S35–S44.
[13] P.P. Edwards, A. Porch, M.O. Jones, D.V. Morgan, R.M. Perks, Basic materials physics of transparent conducting oxides, Dalton Trans. 19 (2004) 2995–3002.
[14] S. Mandal, R.K. Singha, A. Dhar, S.K. Ray, Optical and structural characteristics of ZnO thin films grown by rf magnetron sputtering, Mat. Res. Bull. 43 (2008) 244–250.
[15] B.C. Yadav, K. Agrahari, S. Singh, T.P. Yadav, Fabrication and characterization of nano structured Indium tin oxide film and its application as humidity and gas sensors, J. Mater. Sci.: Mater. Electron 27 (2016) 4172–4179.
[16] A.M. Ganose, D.O. Scanlon, Band gap and work function tailoring of SnO2 for improved transparent conducting ability in photovoltaics, J. Mater. Chem. C 4 (2016) 1467–1475.
[17] X. Yu, T.J. Marks, A. Facchetti, Metal oxide for optoelectronic applications, Nat. Mater. 15 (2016) 383–396.
[18] B.D. Cullity, Elements of X-ray Diffraction, second ed. Addison-Wesley, Massachusetts, 1978.
[19] P. Jonnard, H. Bercegol, L. Lamaignere, J.P. Morreeuw, J.L. Rullier, E. Cotttancin, M. Pellarin, X-ray spectroscopy study of electronic structure of laser-irradiated Au nanoparticles in a silica film, J. Appl. Phys. 97 (2005) 064306.
[20] K.L. Kelly, E. Coronado, L.L. Zhao, G.C. Schatz, The optical properties of metal nanoparticles: the influence of size, shape, and dielectric environment, J. Phys. Chem. B 107 (2003) 668–677.
[21] W. Rechberger, A. Hohenau, A. Leitner, J.R. Krenn, B. Lamprecht, F.R. Aussenegg, Optical properties of two interacting gold nanoparticles, Opt. Commun. 220 (2003) 137–141.

[22] Z. Liu, H. Wang, H. Li, X. Wang, Red shift of plasmon resonance frequency due to the interacting Ag nanoparticles embedded in single crystal SiO_2 by implantation, Appl. Phys. Lett. 72 (1998) 1823–1825.
[23] F. Watt, J.A. Van Kan, I. Rajta, A.A. Bettiol, T.F. Choo, M.B.H. Breese, T. Osipowicz, The National University of Singapore high energy ion nano-probe facility: performance tests, Nucl. Instr. and Meth. B 210 (2003) 14–20.
[24] L. Doolittle, Algorithms for the rapid simulation of Rutherford backscattering spectra, Nucl. Instr. Meth. B 9 (1985) 344–351.
[25] J.C. Fan, J.B. Goodenough, X-ray photoemission spectroscopy studies of Sn-doped indium-oxide films, J. Appl. Phys. 48 (1977) 3524–3531.
[26] A. Gurlo, M. Ivanovskaya, A. Pfau, U. Weimar, W. Gopel, Sol-gel prepared In_2O_3 thin films, Thin Solid Films 307 (1997) 288–293.
[27] D. Cahen, P.J. Ireland, L.L. Kazmerski, F.A. Thiel, X-ray photoelectron and Auger electron spectroscopic analysis of surface treatments and electrochemical decomposition of $CuInSe_2$ photoelectrodes, J. Appl. Phys. 57 (1985) 4761–4771.
[28] R.H. Bube, Photoelectronic Properties of Semiconductors, Cambridge University Press, Cambridge, 1992 p.318.
[29] S.A. Studenikin, N. Golego, M. Cocivera, Optical and electrical properties of undoped ZnO films grown by spray pyrolysis of zinc nitrate solution, J. Appl. Phys. 83 (1998) 2104–2111.
[30] S.T. Pantelides (Ed.), Deep Centers in Semiconductors: A State of the Art Approach, second ed.Gordon and Breach, Switzerland, 1992.
[31] H.J. Queisser, E.E. Haller, Defects in semiconductors: some fatal, some vital, Science 281 (1998) 945–950.
[32] G.D. Watkins, Defects in semiconductors, Mater. Sci. Forum (1994) 143–147.
[33] S. Lany, A. Zunger, Anion vacancies as a source of persistent photoconductivity in II-VI and chalcopyrite semiconductors, Phys. Rev. B 72 (2005) 035215.
[34] S. Lany, A. Zunger, Intrinsic DX centers in ternary chalcopyrite semiconductors, Phys. Rev. Lett. 100 (2008) 016401.
[35] D.M. Hofmann, D. Pfisterer, J. Sann, B.K. Meyer, R. Tena-zaera, V. Munoz-sanjose, T. Frank, G. Pensl, Properties of the oxygen vacancy in ZnO, Appl. Phys. A Mater. Sci. Process. 88 (2007) 147–151.
[36] J.H. Schon, E. Bucher, Persistent photoconductivity in n- and p-type $CuGaSe_2$, J. Phys. D. Appl. Phys. 34 (2001) 25–29.
[37] A. Janotti, C.G. Van de Walle, Oxygen vacancies in ZnO, Appl. Phys. Lett. 87 (2005) 122102.
[38] H.C. Yang, T.Y. Lin, Y.F. Chen, Persistent photoconductivity in InGaN/GaN multiquantum wells, Appl. Phys. Lett. 78 (2001) 338–340.
[39] C. Kisielowski, J. Kruger, S. Ruvimov, T. Suski, J.W. Ager, E. Jones, Z. Liliental-Weber, M. Rubin, E.R. Weber, M.D. Bremser, R.F. Davis, Strain-related phenomena in GaN thin films, Phys. Rev. B 54 (1996) 17745–17753.
[40] B. Pashmakov, B. Claflin, H. Fritzsche, Photoreduction and oxidation of amorphous indium oxide, Solid State Commun. 86 (1993) 619–622.
[41] C. Xirouchaki, G. Kiriakidis, T.F. Pedersen, H. Fritzsche, Photoreduction and oxidation of as-deposited microcrystalline indium oxide, J. Appl. Phys. 79 (1996) 9349–9352.
[42] M. Bender, N. Katsarakis, E. Gagaoudakis, E. Hourdakis, E. Douloufakis, V. Cimalla, G. Kiriakidis, Dependence of the photoreduction and oxidation behavior of indium oxide films on substrate temperature and film thickness, J. Appl. Phys. 90 (2001) 5382–5387.
[43] I. Tanaka, K. Tatsumi, M. Nakano, H. Adachi, F. Oba, First-principles calculations of anion vacancies in oxides and nitrides, J. Am. Ceram. Soc. 85 (2002) 68–74.
[44] P. Malar, B.C. Mohanty, S. Kasiviswanathan, Growth and Rutherford backscattering spectrometry study of direct current sputtered indium oxide films, Thin Solid Films 488 (2005) 26–33.